

High Fermi velocities and small cyclotron masses in LaAlGe

Zhixiang Hu,^{1,2} Qianheng Du,^{1,2} Yu Liu,^{1,¶} D. Graf,³ and C. Petrovic^{1,2,‡}

¹Condensed Matter Physics and Materials Science Department,
Brookhaven National Laboratory, Upton, New York 11973, USA

²Department of Materials Science and Chemical Engineering,
Stony Brook University, Stony Brook, New York 11790, USA

³National High Magnetic Field Laboratory, Florida State University, Tallahassee,
Florida 32306-4005, USA

(Dated: 10 December 2020)

We report quantum oscillation measurements of LaAlGe, a Lorentz-violating type-II Weyl semimetal with tilted Weyl cones. Very small quasiparticle masses and very high Fermi velocities were detected at the Fermi surface. Whereas three main frequencies have been observed, angular dependence of two Fermi surface sheets indicates possible two-dimensional (2D) character despite the absence of the 2D structural features such as van der Waals bonds. Such conducting states may offer a good platform for low-dimensional polarized spin current in magnetic RAlGe (R = Ce, Pr) materials.

Unlike normal semimetals, topological Dirac semimetals have surface states which are induced by topology of the bulk.^{1,2} The states can be described by linear energy dispersion near Dirac points in the Brillouin zone with very small effective mass and high carrier mobility. In crystals additional symmetry breaking turns Dirac points into pairs of Weyl nodes with distinct chirality that are separated in momentum space. Surface states connecting two different Weyl nodes form Fermi arcs whereas Weyl nodes represent monopoles of Berry curvature, giving rise to unusual electronic transport phenomena.³⁻⁷

This is of interest for a broad range of applications.^{8,9} The type-II Weyl semimetals with tilted Weyl cones in three-dimensional (3D) bulk crystals attract considerable attention due to tilted dispersion; the Fermi surface features electron and hole pockets that touch at the Weyl node.¹⁰⁻¹⁴ The dispersion violates Lorentz symmetry and gives rise to tunable properties that could be used in room-temperature optoelectronics, valley filtering and photodetector fabrication.¹⁵⁻²² Of particular interest are optical applications similar to graphene; topological semimetal crystals host Dirac surface plasmon polariton and allow for propagation of electromagnetic modes in a waveguide geometry.²³⁻²⁶

LaAlGe features type-II Weyl nodes.²⁷⁻²⁹ Thin films of LaAlGe show metallic resistivity, small residual resistivity ratio $RRR = \rho(300\text{ K})/\rho(5\text{ K}) = 1.17$, relatively high residual resistivity of about $87\ \mu\Omega\text{ cm}$, single band electronic transport and $7 \times 10^{21}\text{ cm}^{-3}$ carrier concentration at 5 K.³⁰ In particular, contribution of Weyl points at the Fermi surface, dimensionality and characteristics of such states are important. Here we perform quantum oscillation studies of LaAlGe. Our results indicate that rather small effective masses and high Fermi velocities of tilted type-II Weyl cones are dominant in electronic transport. We also present evidence for quasi-2D Fermi surface states despite the absence of van der Waals gap or other two-dimensional atomic units in the crystal structure. LaAlGe Fermi surface can be further tuned in magnetic members of RAlGe family (R = Ce, Pr) since they are ferromagnets where Zeeman field could be treated as

a coupling without altering the low-energy band structure of LaAlGe.²⁷

Single crystals of LaAlGe were grown by high temperature self-flux method.³¹ La, Ge and Al were mixed in a ratio of 1:1:20 in an alumina crucible and sealed in a vacuum inside a quartz tube. The ampoule was heated to $1175\text{ }^\circ\text{C}$ for 55 hours and kept there for two hours. Shiny crystals of about $2\text{ mm} \times 2\text{ mm} \times 0.5\text{ mm}$ were decanted from liquid at $700\text{ }^\circ\text{C}$ after one week of cooling. Excess residual flux was cleaned by polishing before measurements. Powder X-ray diffraction (XRD) was performed on crushed crystal at room temperature by using Cu-K α ($\lambda = 0.15418\text{ nm}$) radiation in a Rigaku Miniflex powder diffractometer. Resistivity was measured by conventional four-wire method in a Quantum Design PPMS-9. Small cuboid specimen were taken to National High Magnetic Field Laboratory (NHMFL) for measurements of temperature and angular dependent de Haas-van Alphen (dHvA) oscillations, where the field ranged from 0 to 35 Tesla. The crystals were mounted onto miniature Seiko piezoresistive cantilevers which were installed on a rotating platform. The field direction can be changed continuously between parallel ($\theta = 0^\circ$) and perpendicular ($\theta = 90^\circ$) to the c -axis of the crystal.

Powder XRD confirms phase purity [Fig. 1(a)]. The unit cell [Fig. 1(a) inset] can be indexed into $I4_1md$ (109) space group with lattice parameters $a = b = 0.4339(3)\text{ nm}$, $c = 1.4821(2)\text{ nm}$ in agreement with reported values.³² The crystal structure is derived from the α -ThSi₂ $I4_1/amd$ prototype where La replaces Th and Ge, Al take the place of Si.³³

The electric resistivity [Fig.1(b)] is metallic and, in the absence of magnetic field, it is explained well by the dominant phonon scattering via Bloch-Grüneisen formula:

$$\rho(T) = \rho_0 + A \left(\frac{T}{\theta_D} \right)^n \int_0^{\theta_D/T} \frac{z^5}{(e^z - 1)(1 - e^{-z})} dz,$$

where $\theta_D = 245(8)\text{ K}$ is the Debye Temperature, $\rho_0 = 8.67(5)\ \mu\Omega\text{ cm}$ is residual resistivity. Whereas LaAlGe

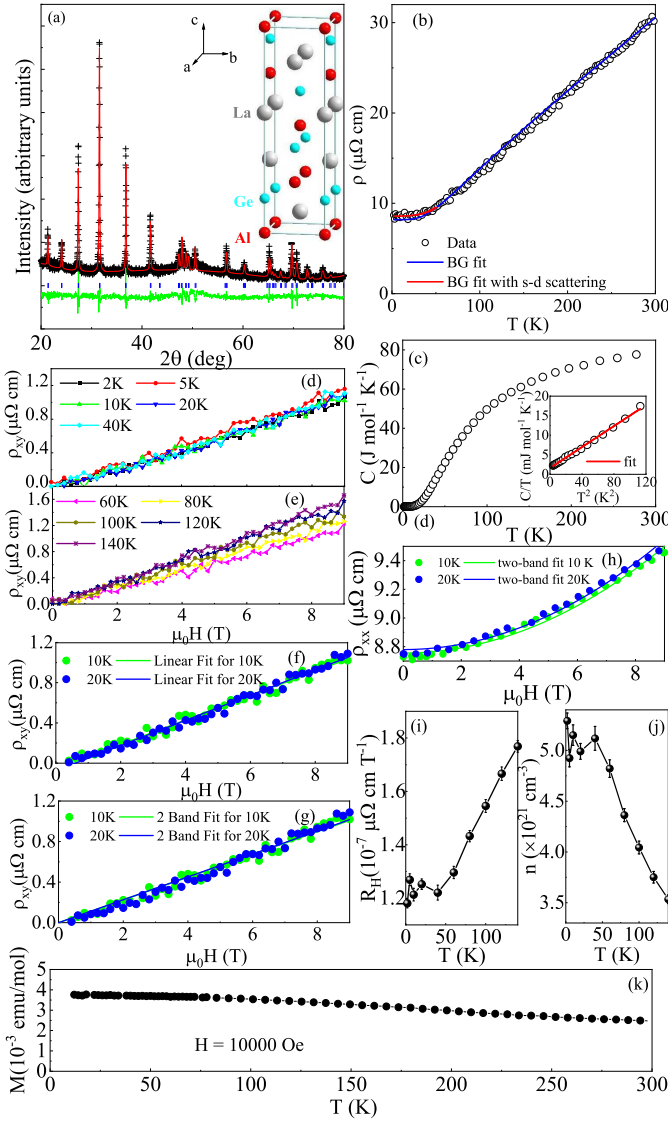


FIG. 1. (Color online). (a) Powder XRD pattern of LaAlGe at room temperature: data (+), structural model (red solid line), difference curve (green solid line, offset for clarity). The vertical tick marks represent Bragg reflections of the $I4_1/amd$ space group. Inset shows crystal structure of LaAlGe. (b) Resistivity $\rho(T)$ of LaAlGe; blue and red lines shows fitting using Bloch-Grüneisen (BG) model (see text). (c) Heat capacity of LaAlGe with Debye model fit (inset). (d,e) Hall resistivity ρ_{xy} measured perpendicular to the current and field out of plane and at different temperatures. Single-band (f) fits of the Hall data. Two-band fits of the magnetic-field dependent ρ_{xy} (g) and resistivity ρ_{xx} (h) at 10 K and 20 K. Hall coefficient R_H (i), and carrier density (j) within the single-band approximation (see text). (k) Magnetization of LaAlGe in 10 kOe magnetic field.

resistivity is well explained by dominant phonon scattering down to 50 K with $n = 5$, at lower temperatures $n = 3$ provides better fit. In the low temperature limit, Bloch-Grüneisen formula could be approximated with $\rho = \rho_0 + AT^n$. Fit to our data [Fig. 1(b) red curve]

gives $\rho_0 = 8.58(5)\mu\Omega \times \text{cm}$ and $n = 3.2(1)$. $n \sim 3$ indicates the Bloch-Wilson limit, where $n = 3$ due to s - d interband scattering. $\text{RRR} = 3.4$ confirms somewhat higher degree of crystalline order when compared to thin films.³⁰ Heat capacity $C(T)$ is shown in Fig. 1(c). The fitting of the low-temperature data using $C = \gamma T + \beta T^3$ gives $\beta = 0.134(2) \text{ mJ mole}^{-1} \text{ K}^{-4}$ and $\gamma = 1.6(1) \text{ mJ mole}^{-1} \text{ K}^{-2}$. The Debye temperature $\Theta_D = 243(1) \text{ K}$ is obtained from $\Theta_D = (12\pi^4 NR/5\beta)^{1/3}$ where N is the atomic number in the chemical formula and R is the universal gas constant. The obtained Debye temperature shows excellent agreement with Bloch-Grüneisen fit results, indicating dominant phonon scattering of $\rho(T)$ where most phonon modes take part.

Hall resistivity ρ_{xy} [Fig. 1(d,e)] is nearly linear in magnetic field suggesting that electronic bands at the Fermi surface are probably compensated with similar overall electron and hole concentration and with similar mobilities.^{27,28,34} In the simplest approximation temperature-dependent Hall coefficient R_H could be estimated from linear data fits ρ_{xy} vs. H , as shown in [Fig.1(f)]. On the other hand, it is likely that LaAlGe features multiband electronic transport, as expected for Weyl semimetals.^{27,28,35}

$$\rho_{xx} = \frac{(n_e\mu_e + n_h\mu_h) + \mu_e\mu_h(n_e\mu_h + n_h\mu_e)B^2}{(n_e\mu_e + n_h\mu_h)^2 + \mu_e^2\mu_h^2(n_h - n_e)^2B^2} \times \frac{1}{e},$$

$$\rho_{xy} = \frac{(n_h\mu_h^2 - n_e\mu_e^2) + \mu_e^2\mu_h^2(n_h - n_e)B^2}{(n_e\mu_e + n_h\mu_h)^2 + \mu_e^2\mu_h^2(n_h - n_e)^2B^2} \times \frac{B}{e},$$

where n_e, n_h, μ_e, μ_h are carrier densities and mobilities of electron and hole-type carriers. Electron-hole compensation $n_e = n_h = n$ further simplifies to:

$$\rho_{xx} = \frac{1}{ne(\mu_e + \mu_h)} + \frac{\mu_e\mu_h}{ne(\mu_e + \mu_h)}B^2,$$

$$\rho_{xy} = \frac{\mu_h - \mu_e}{ne(\mu_h + \mu_e)}B.$$

By fitting magnetic-field dependent ρ_{xy} [Fig. 1(g)] and ρ_{xx} [Fig. 1(h)] we obtain $\mu_e = 262(1) \text{ cm}^2\text{V}^{-1}\text{s}^{-1}$, $\mu_h = 400(7) \text{ cm}^2\text{V}^{-1}\text{s}^{-1}$, $n_e = 1.08(1) \times 10^{21} \text{ cm}^{-3}$ and $n_h = 1.08(2) \times 10^{21} \text{ cm}^{-3}$ at 10K. Likewise, we obtain $\mu_e = 265(1) \text{ cm}^2\text{V}^{-1}\text{s}^{-1}$, $\mu_h = 398(8) \text{ cm}^2\text{V}^{-1}\text{s}^{-1}$, $n_e = 1.06(1) \times 10^{21} \text{ cm}^{-3}$ and $n_h = 1.06(2) \times 10^{21} \text{ cm}^{-3}$ at 20K. Therefore due to compensated Fermi surface pockets, temperature-dependent Hall coefficient and carrier density n could be approximated with the single band model [Fig. 1(i,j)] where e is electronic charge, $R_H = \frac{1}{ne}$ and R_H is the slope of ρ_{xy} [Fig. 1(d,e)]. Carrier concentration shows reduction above 40 K and is consistent with result obtained in thin films.³⁰ This is coincident with increased resistivity [Fig. 1(b)] above 40 K, indicating that $\rho(T)$ is also influenced by changes in n , in addition to phonon-related scattering induced by increased

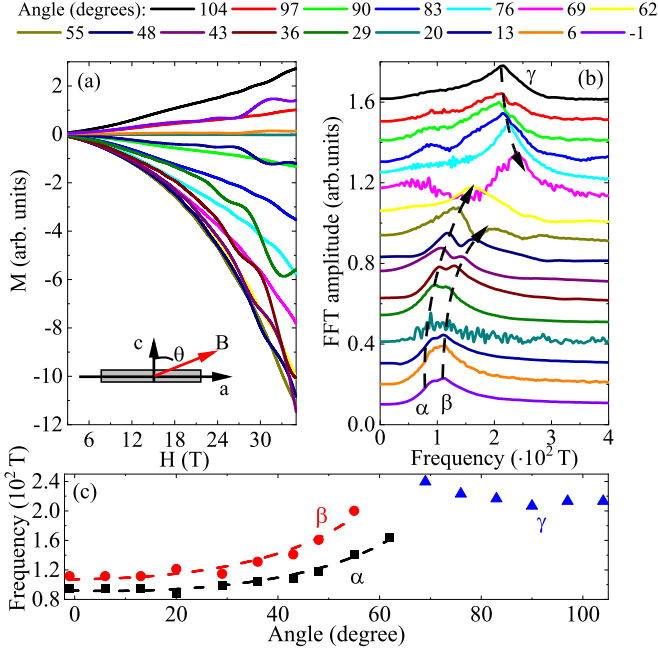


FIG. 2. (Color online). (a) Angle-dependent dHvA oscillations. LaAlGe crystal installed on cantilever is rotated from -14° to 91° with data collected approximately every 7° ; (b) Fourier transform spectrum of oscillations at different angles (c) Traces of frequencies α and β as a function of the angle are well fitted to quasi-2D model $\sim 1/\cos\theta$.

vibrations. Magnetization of LaAlGe is paramagnetic, somewhat enhanced at low temperatures [Fig. 1(k)].

Angle-dependent de Haas-van Alphen oscillations [Fig.2(a)] appear at all angles above 8 T. Figure 2(b) plots the angular evolution of Fast Fourier Transform (FFT) frequencies. Clear traces of three frequencies α , β and γ are plotted individually in Fig.2(b,c). Frequencies α and β increase continuously above about 0° . The γ frequency can be traced in a relatively narrow range between 70° and 110° and can not be fitted by either ellipsoidal or two-dimensional model. On the other hand, angular-dependence of F_α and F_β is well fitted by the two-dimensional model $F(\theta) = A/\cos(\theta)$ where A is a constant.³⁶ This observation is consistent with the possible quasi-2D Fermi surface sheets.

Temperature dependent dHvA oscillations are also observed above 10 T in all magnetic fields [Fig. 3(a)]. Oscillation component and Fourier transform of dHvA oscillations [Fig. 3(b,c)] reveal clear signature of two frequencies, $F_\alpha = 91.9(1)$ T and $F_\beta = 108.3(1)$ T consistent with Fig. 2. This shows that multiple but closed Fermi surfaces exist in the ab -plane whose relation with frequencies is given by Onsager formula $F = (\hbar/2\pi e)A$ where A is the cross-section area of Fermi surface perpendicular to the field: $A_\alpha = 0.87(1)$ nm $^{-2}$ and $A_\beta = 1.03(1)$ nm $^{-2}$.

The oscillatory component of electronic system with Dirac points in magnetic field is described by the Lifshitz-Kosevich formula with the Berry phase:³⁷

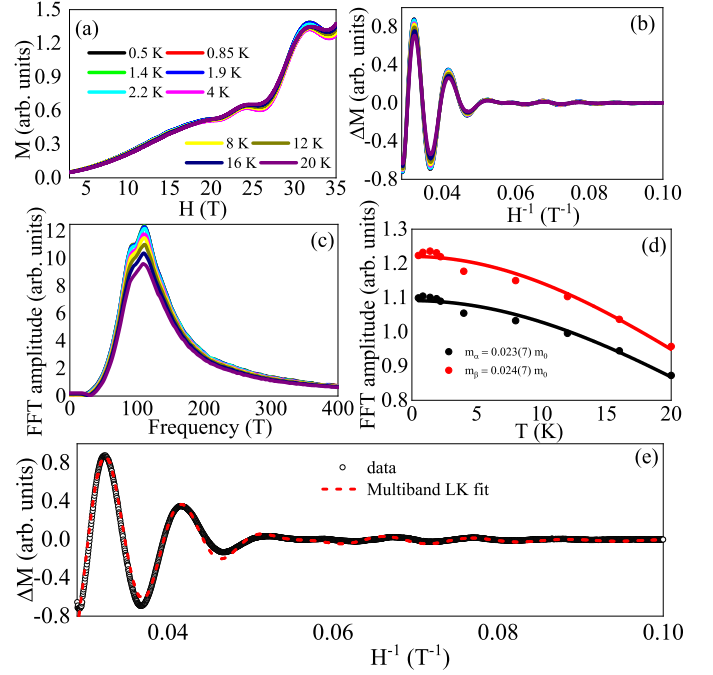


FIG. 3. (Color online). Cantilever magnetization of LaAlGe at different temperatures with magnetic field applied along the c -axis (a) and dHvA oscillatory components obtained by smooth background subtraction (b). Fast Fourier transform spectra for dHvA (c). FFT amplitude vs temperature; LK fits are shown with the solid lines (see text). (e) Oscillatory magnetization at 0.5 K solid lines are fit of The red solid line represents the multiband LK fit.

$$\Delta M \propto -B^\lambda R_T R_D R_S \sin 2\pi[(F/B) - \gamma - \delta],$$

The $R_T = \alpha m^* T / H \sinh(\alpha m^* T / H)$, $R_D = \exp(-\alpha m^* T_D / H)$ and $R_S = \cos(\pi g m^* / 2)$ where $m^* = m/m_e$ is the effective mass of the cyclotron orbit, T_D is the Dingle temperature and $\alpha = 2\pi^2 k_B / e\hbar \approx 14.69$ T/K. The exponent $\lambda = 0$ for 2D and $1/2$ for 3D Fermi surface sheets. The argument of the oscillatory sine function contains phase factor $(-\gamma - \delta)$ in which $\delta = 0$ for 2D Fermi surface and $\gamma = (1/2) - \phi_B / 2\pi$ where ϕ_B is the Berry phase. Fits of the oscillation amplitude temperature dependence to the thermal damping factor R_T [Fig. 3(d)] gives effective masses $m_\alpha^* = 0.023(7)m_0$ and $m_\beta^* = 0.024(7)m_0$.

Since dominant Fermi surface sheets are quasi-2D, Fermi velocity $v_F = \hbar k_F / m^*$ could be estimated from the quasiparticle masses and Fermi wavevector k_F which is related to the circular cross-section area of the Fermi surface as $A = \pi k_F^2$. For F_α and F_β calculations give $k_{F,\alpha} = 0.053(1)$ \AA^{-1} , $k_{F,\beta} = 0.057(1)$ \AA^{-1} , $v_{\alpha} = 2.66(1) \times 10^6$ m/s and $v_{\beta} = 2.77(1) \times 10^6$. These are large Fermi velocities, somewhat higher when compared to velocities near tilted Dirac cone-associated W_2 points measured in angular resolved photoemission (ARPES)²⁸ but on the

other hand they are comparable to SrMnBi₂ and canonical Weyl semimetals WTe₂ or NbP (Table I).^{36,38,39}

Weyl Semimental	Effective Mass	Velocity
LaAlGe α	$0.023m_0$	2.66×10^6 m/s
LaAlGe β	$0.024m_0$	2.77×10^6 m/s
SrMnBi ₂	$0.29m_0$	5.13×10^5 m/s ³⁶
WTe ₂ α	$0.412m_0$	3.09×10^5 m/s ³⁸
WTe ₂ β	$0.482m_0$	
NbP	$0.1m_0$	1.8×10^5 m/s ³⁹

TABLE I. Comparison of Weyl semimetal LaAlGe, SrMnBi₂, WTe₂, NbP

Multiple frequency oscillations are well treated by the linear superposition of several single-frequency oscillations using multiband LK formula for data taken at 0.5 K.^{40–43} The fit [Fig. 3(e)] yields Berry phase for different Fermi surface sheets $\phi_{B,\alpha} = 0.88(1)\pi$ for F_α and $\phi_{B,\beta} = 0.96(1)\pi$ for F_β . Topologically non-trivial Berry phases confirm the linear dispersion of Weyl fermions for the observed Fermi surface pockets.

The fitted Dingle temperatures are $T_{D,\alpha} = 159(4)$ K and $T_{D,\beta} = 336(4)$ K. From $T_D = \frac{\hbar}{2\pi k_B \tau_Q}$ we evaluate scattering rate $\tau_\alpha = 7.64(1) \times 10^{-15}$ s and $\tau_\beta = 3.62(1) \times 10^{-15}$ s. Mobility estimate using $\mu = e\tau/m^*$ gives $\mu_\alpha = 584(1)$ cm²V⁻¹s⁻¹ and $\mu_\beta = 265(1)$ cm²V⁻¹s⁻¹; when compared to mobility estimate from Hall effect at 10 K (Fig. 1) this could imply somewhat higher temperature dependence of the hole pocket.

Very small effective masses are consistent with Weyl points in LaAlGe Fermi surface. Since other Weyl points are 60 meV to 130 meV away from the Fermi level, the quasi-2D Fermi surface parts that correspond to observed frequencies F_α , F_β but also F_γ should correspond to some of the type-II W_2 Weyl cones with tilted dispersion away from the k_z plane.²⁸

We estimate electronic specific heat from the effective mass obtained in quantum oscillation experiment using quasi-two-dimensional approximation:⁴⁴

$$\gamma_N = \sum_i \frac{\pi N_A k_B^2 a b}{3\hbar^2} m^*$$

where $a = b = 0.4339(2)$ are the tetragonal plane lattice parameters, m^* is the quasiparticle mass, N_A is Avogadro's number, k_B is Boltzmann's constant and \hbar is Planck's constant. From the sum over all Fermi pockets which include four W_2 s on the top of Brillouin zone for α and four on top for β frequencies, four W_2 s on the bottom for α and four for β , $\gamma_N = 0.70(5)(1)$ mJ mol⁻¹ K⁻² can be obtained.²⁸ This is less than the value obtained from fits in [Fig. 1(c)] and indicates that not all portions of Fermi surface detected in quantum oscillations contribute to electronic specific heat.

In summary we showed that LaAlGe features electronic transport dominated by Weyl nodes with very small effective masses and high Fermi velocities. The dominant

type-II Weyl cones at the Fermi surface are possibly quasi-2D, despite the absence of two-dimensional crystallographic units as in materials with van der Waals bonds. Such conducting states coupled with magnetic moments are stable in the presence of long-range Coulomb interactions,^{27,45} which points to possibility of robust spin polarized currents in future devices.

Work at Brookhaven National Laboratory was supported by US DOE, Office of Science, Office of Basic Energy Sciences under contract DE-SC0012704. A portion of this work was performed at the National High Magnetic Field Laboratory, which is supported by the National Science Foundation Cooperative Agreement No. DMR-1644779 and the State of Florida.

[¶] Present address: Los Alamos National Laboratory, MS K764, Los Alamos NM 87545 [‡] petrovic@bnl.gov

I. DATA AVAILABILITY

The data that support the findings of this study are available from the corresponding author upon reasonable request.

- ¹T.O. Wehling, A.M. Black-Schaffer and A. V. Balatsky, *Advances in Physics* **63**, 1 (2014).
- ²M. Z. Hasan and C. L. Kane, *Rev. Mod. Phys.* **82**, 3045 (2010).
- ³H. Weyl, *Z. Phys.* **5**, 378 (2009).
- ⁴Xiangang Wan, Ari M. Turner, Ashvin Vishwanath, and Sergey Y. Savrasov, *Phys. Rev. B* **83**, 205101 (2011).
- ⁵B. Q. Lv, H. M. Weng, B. B. Fu, X. P. Wang, H. Miao, J. Ma, P. Richard, X. C. Huang, L. X. Zhao, G. F. Chen, Z. Fang, X. Dai, T. Qian, and H. Ding, *Phys. Rev. X* **5**, 031013 (2015).
- ⁶Cheng-Long Zhang, Su-Yang Xu, Ilya Belopolski, Zhujun Yuan, Ziquan Lin, Bingbing Tong, Guang Bian, Nasser Alidoust, Chi-Cheng Lee, Shin-Ming Huang, Tay-Rong Chang, Guoqing Chang, Chuang-Han Hsu, Horng-Tay Jeng, Madhab Neupane, Daniel S. Sanchez, Hao Zheng, Junfeng Wang, Hsin Lin, Chi Zhang, Hai-Zhou Lu, Shun-Qing Shen, Titus Neupert, M. Zahid Hasan and Shuang Jia, *Nature Communications* **7**, 10735 (2016).
- ⁷Binghai Yan and Claudia Felser, *Annu. Rev. Cond. Matt. Phys.* **8**, 337 (2017).
- ⁸C. R. Rajamathi, U. Gupta, N. Kumar, H. Yang, Y. Sun, V. Süß, C. Shekhar, M. Schmidt, H. Blumtritt, P. Werner, B. Yan, S. Parkin, C. Felser, and C. N. R. Rao, *Adv. Mater.* **29**, 1606202 (2017).
- ⁹Ching-Kit Chan, Patrick A. Lee, Kenneth S. Burch, Jung Hoon Han and Ying Ran, *Phys. Rev. Lett.* **116**, 026805 (2016).
- ¹⁰A. A. Soluyanov, D. Gresch, Zhijun Wang, QuanSheng Wu, M. Troyer, Xi Dai and A. Bernevig, *Nature* **527**, 495 (2015).
- ¹¹E. J. Bergholtz, Zhao Liu, M. Trescher, R. Moessner, and M. Udagawa, *Phys. Rev. Lett.* **114**, 016806 (2015).
- ¹²Maximilian Trescher, Björn Sbierski, Piet W. Brouwer, and Emil J. Bergholtz, *Phys. Rev. B* **91**, 115135 (2015).
- ¹³Mazhar N. Ali, Jun Xiong, Steven Flynn, Jing Tao, Quinn D. Gibson, Leslie M. Schoop, Tian Liang, Neel Haldolaarachchige, Max Hirschberger, N. P. Ong and R. J. Cava, *Nature* **514**, 205 (2014).
- ¹⁴Raditya Weda Bomantara and Jiangbin Gong, *Phys. Rev. B* **94**, 235447 (2016).
- ¹⁵Shumeng Chi, Zhilin Li, Ying Xie, Yongguang Zhao, Zeyan Wang, Lei Li, Haohai Yu, Gang Wang, Hongming Weng, Huaijin Zhang and Jiyang Wang, *Adv. Mater.* **30**, 1801372 (2018).
- ¹⁶Ching-Kit Chan, Netanel H. Lindner, Gil Refael, and Patrick A. Lee, *Phys. Rev. B* **95**, 041104 (2017).

- ¹⁷E. J. Sie, C. M. Nyby, C. D. Pemmaraju, S. J. Park, X. Shen, J. Yang, M. C. Hoffmann, B. K. Ofori-Okai, R. Li, A. H. Reid, S. Weathersby, E. Mannebach, N. Finney, D. Rhodes, D. Chenet, A. Antony, L. Balicas, J. Hone, T. P. Devereaux, T. F. Heinz, X. Wang, and A. M. Lindenberg, *Nature* **565**, 61 (2019).
- ¹⁸Can Yesilyurt, Zhuo Bin Siu, Seng Ghee Tan, Gengchiao Liang, Shengyuan A. Yang and Mansoor B.A. Jalil, *Scientific Reports* **9**, 4480 (2019).
- ¹⁹M. Y. Zhang, Z. X. Wang, Y. N. Li, L. Y. Shi, D. Wu, T. Lin, S. J. Zhang, Y. Q. Liu, Q. M. Liu, J. Wang, T. Dong and N. L. Wang, *Phys. Rev. X* **9**, 021036 (2019).
- ²⁰Kaixuan Zhang, Yongping Du, Zeming Qi, Bin Cheng, Xiaodong Fan, Laiming Wei, Lin Li, Dongli Wang, Guolin Yu, Shuhong Hu, Changhong Sun, Zhiming Huang, Junhao Chu, Xiangang Wan, and Changgan Zeng, *Phys. Rev. Applied* **13**, 014058 (2020).
- ²¹Shuyuan Shi, Shiheng Liang, Zhifeng Zhu, Kaiming Cai, Shawn D. Pollard, Yi Wang, Junyong Wang, Qisheng Wang, Pan He, Jiawei Yu, Goki Eda, Gengchiao Liang and Hyunsoo Yang, *Nature Nanotechnology* **14**, 945 (2019).
- ²²SV. Hung Nguyen and J.-C. Charlier, *Phys. Rev. B* **97**, 235113 (2018).
- ²³Anmol Thakur, Krishanu Sadhukhan, and Amit Agarwal, *Phys. Rev. B* **97**, 035403 (2018).
- ²⁴O. V. Kotov and Yu. E. Lozovik, *Phys. Rev. B* **93**, 235417 (2016).
- ²⁵Z. Jalali-Mola and S. A. Jafari, *Phys. Rev. B* **100**, 205413 (2019).
- ²⁶Heng Li, Jhu-Hong Li, Kuo-Bin Hong, Min-Wen Yu, Yi-Cheng Chung, Chu-Yuan Hsu, Jhen-Hong Yang, Chang-Wei Cheng, Zhen-Ting Huang, Kuo-Ping Chen, Tzy-Rong Lin, Shangjr Gwo, and Tien-Chang Lu, *Nano Lett.* **19**, 5017 (2019).
- ²⁷Guoqing Chang, Bahadur Singh, Su-Yang Xu, Guang Bian, Shin-Ming Huang, Chuang-Han Hsu, Ilya Belopolski, Nasser Alidoust, Daniel S. Sanchez, Hao Zheng, Hong Lu, Xiao Zhang, Yi Bian, Tay-Rong Chang, Horng-Tay Jeng, Arun Bansil, Han Hsu, Shuang Jia, Titus Neupert, Hsin Lin, and M. Zahid Hasan, *Phys. Rev. B* **97**, 041104 (2018).
- ²⁸Su-Yang Xu, Nasser Alidoust, Guoqing Chang, Hong Lu, Bahadur Singh, Ilya Belopolski, Daniel S. Sanchez, Xiao Zhang, Guang Bian, Hao Zheng, Marious-Adrian Husanu, Yi Bian, Shin-Ming Huang, Chuang-Han Hsu, Tay-Rong Chang, Horng-Tay Jeng, Arun Bansil, Titus Neupert, Vladimir N. Strocov, Hsin Lin, Shuang Jia and M. Zahid Hasan, *Sci. Adv.* **3**, e1603266 (2017).
- ²⁹M. Udagawa and E. J. Bergholtz, *Phys. Rev. Lett.* **117**, 086401 (2016).
- ³⁰Niraj Bhattarai, Andrew W. Forbes, Rajendra P. Dulal, Ian L. Pegg and John Philip, *MRS Communications* **10**, 272 (2020).
- ³¹Z. Fisk and J.P. Remeika, Growth of single crystals from molten metal fluxes, in *Handbook on the Physics and Chemistry of Rare Earths*, K.A. Gschneidner Jr and L. Eyring, eds., Vol. 12, Elsevier, Amsterdam, 1989, p.53. **65**, 1117 (1992).
- ³²J. T. Zhao and E. Parthé, *Acta Crystallogr. C* **46**, 2276 (1990).
- ³³F. Kneidinger, H. Michor, A. Sidorenko, E. Bauer, I. Zeiringer, P. Rogl, C. Blaas-Schener, D. Reith, and R. Podloucky, *Phys. Rev. B* **88**, 104508 (2013).
- ³⁴Qi Wang, Qiangwei Yin and Hechang Lei, *J. Phys. Condens. Matt.* **32**, 015601 (2020).
- ³⁵Aifeng Wang, D. Graf, Yu Liu, Qianheng Du, Jiabao Zheng, Hechang Lei, and C. Petrovic, *Phys. Rev. B* **96**, 121107 (2017).
- ³⁶Kefeng Wang, D. Graf, Hechang Lei, S. W. Tozer, and C. Petrovic, *Phys. Rev. B* **84**, 220401(R) (2011).
- ³⁷David Shoenberg, *Magnetic oscillations in metals*. Cambridge university press, 2009.
- ³⁸Peng Li, Yan Wen1, Xin He, Qiang Zhang, Chuan Xia, Zhi-Ming Yu, Shengyuan A. Yang, Zhiyong Zhu, Husam N. Alshareef and Xi-Xiang Zhang, *Nature Communications* **8**, 2150 (2017).
- ³⁹Zhen Wang, Yi Zheng, Zhixuan Shen, Yunhao Lu, Hanyan Fang, Feng Sheng, Yi Zhou, Xiaojun Yang, Yupeng Li, Chunmu Feng, and Zhu-An Xu, *Phys. Rev. B* **93**, 121112 (2016).
- ⁴⁰J. Hu, Z. Tang, J. Liu, X. Liu, Y. Zhu, D. Graf, K. Myhro, S. Tran, C. N. Lau, J. Wei, and Z. Mao, *Phys. Rev. Lett.* **117**, 016602 (2016).
- ⁴¹J. Hu, J. Y. Liu, D. Graf, S. M. A. Radmanesh, D. J. Adams, A. Chuang, Y. Wang, I. Chiorescu, J. Wei, L. Spinu, and Z. Q. Mao, *Sci. Rep.* **6**, 18674 (2016).
- ⁴²Jin Hu, Zhijie Tang, Jinyu Liu, Yanglin Zhu, Jiang Wei, and Zhiqiang Mao, *Phys. Rev. B* **96**, 045127 (2017).
- ⁴³Sheng Xu, Jian-Feng Zhang, Yi-Yan Wang, Lin-Lin Sun, Huan Wang, Yuan Su, Xiao-Yan Wang, Kai Liu, and Tian-Long Xia, *Phys. Rev. B* **99**, 115138 (2019).
- ⁴⁴N. Kikugawa, A. W. Rost, C. W. Hicks, A. J. Schofield, and A. P. Mackenzie, *J. Phys. Soc. Jpn.*, **79**, 024704 (2010).
- ⁴⁵Yu-Li Lee and Yu-Wen Lee, *Phys. Rev. B* **97**, 035141 (2018).